Geophysical Research Letters

RESEARCH LETTER
10.1029/2020GL089077

Key Points:

- The ground-based transmitter in northwest Australia scatters electrons into the drift loss cone
- The Energetic Particle Telescope on the PROBA-V satellite sees enhanced fluxes at 500–800 keV from low-Earth orbit
- The enhanced fluxes occur at energy-dependent L-shells that are consistent with the resonance condition for ducted and nonducted waves

Correspondence to:
G. S. Cunningham,
cunning@lanl.gov

Citation:
Cunningham, G. S., Botek, E., Pierrard, V., Cully, C., & Ripoll, J.-F. (2020). Observation of high-energy electrons precipitated by NWC transmitter from PROBA-V low-Earth orbit satellite. *Geophysical Research Letters*, *47*, e2020GL089077. https://doi.org/10.1029/2020GL089077

Received 28 MAY 2020
Accepted 10 JUL 2020
Accepted article online 17 JUL 2020

Observation of High-Energy Electrons Precipitated by NWC Transmitter From PROBA-V Low-Earth Orbit Satellite

G. S. Cunningham[1], E. Botek[2], V. Pierrard[2,3], C. Cully[4], and J.-F. Ripoll[5,6]

[1]Space Science and Applications, ISR-1, Los Alamos National Laboratory, Los Alamos, NM, USA, [2]Royal Belgian Institute for Space Aeronomy, Space Physics, 3 av. Circulaire, Brussels, Belgium, [3]Université Catholique de Louvain (UCLouvain), Center for Space Radiations (CSR) and Georges Lemaître Centre for Earth and Climate Research (TECLIM), Earth and Life Institute (ELI), Place Louis Pasteur 3 bte L4.03.08, Louvain-La-Neuve, Belgium, [4]Department of Physics and Astronomy, University of Calgary, Calgary, Alberta, Canada, [5]CEA, DAM, DIF, F-91297, Arpajon, France, [6]UPS, CEA, LMCE, 91680, Bruyères-le-Châtel, France

Abstract The very low-frequency transmitter in the Northwest Cape of Australia (NWC) has previously been observed to pitch-angle scatter electrons with energies from 30–400 keV, creating enhanced fluxes measured by low-Earth orbiting (LEO) satellites. Here we use observations from the Energetic Particle Telescope on PROBA-V. We compare the measured flux, as a function of local magnetic field strength, when the NWC transmitter is "on" versus "off," and find enhanced fluxes only when NWC is "on" and located on the nightside. The enhanced fluxes occur in the population gradually transitioning from "permanently trapped" to "quasi-trapped." We show that electrons up to 800 keV, substantially higher energy than previously studied, are scattered by resonant interactions with NWC to produce enhanced fluxes. The enhanced fluxes appear at multiple L-shells for each energy channel, consistent with resonance conditions at distinct wave normal angles, that indicate ducted interactions at $L < 1.55$ and unducted interactions at $L > 1.65$.

Plain Language Summary Radio waves with a low enough frequency can reflect off Earth's surface as well as the ionosphere, a layer of charged particles above Earth's atmosphere created by the Sun's ionization of the upper atmosphere. These waves bounce back and forth in the Earth-ionosphere waveguide, enabling AM (Amplitude Modulation) radio to be heard at large distances, for example. Transmitters with even lower frequencies than AM radio, in the tens of kiloHertz range, are used to communicate with submarines just below the ocean's surface that can be located on the other side of the world. The ionosphere is not a perfect reflector, though, and some of the transmitter wave power escapes into Earth's magnetosphere, a region where charged particles like electrons can be trapped for many months on magnetic field lines. The radio waves can scatter the trapped electrons into Earth's atmosphere, where they rapidly lose energy and no longer pose a threat to space-based assets. Understanding how naval transmitters scatter trapped electrons is needed to help us explain why electrons stay trapped for as long as they do, and enable us to predict radiation damage to the growing number of satellites that orbit Earth with low altitudes, which limits the satellite's useful lifetime.

1. Introduction

High-energy electrons trapped in Earth's inner radiation belt have decay times as long as hundreds of days, compared to the outer belt of high-energy electrons that have decay times of days to tens of days (Claudepierre et al., 2020). The source and loss mechanisms that control the inner-belt electron population are still being investigated (Albert et al., 2020; Claudepierre et al., 2020; Ross et al., 2019), despite the fact that the first model to explain the two-belt structure of trapped electrons was published almost 50 years ago (Lyons & Thorne, 1973). Abel and Thorne (1998) quantified the role that pitch-angle scattering from lightning-generated whistlers (LGW) and Navy ground-based transmitters needed to play to explain the observed decay times at low L-shell observed after the Starfish Prime high-altitude nuclear explosion. These early models used assumptions based on the often sparse observational record available at that time for the wave properties and plasmasphere (cf. review in Ripoll et al., 2020). These assumptions have since

been refined by a number of authors using space-based measurements, most recently from the NASA Van Allen Probes mission (Mauk et al., 2012). The most recent work predicts decay times that are either substantially larger than the observations in the inner belt at MeV energies (Ross et al., 2019) or have a large uncertainty due to how the LGW and ground-based transmitters propagate through the ionosphere and into the magnetosphere and/or the state of the background plasmasphere (Albert et al., 2020; Starks et al., 2020).

Ground-based very low-frequency (VLF) transmitters present an opportunity to validate the use of quasilinear theory for wave-particle interactions by comparing predictions of pitch-angle scattering to observational data in a situation in which the wave properties and background magnetic field and cold plasma properties are well known. Sauvaud et al. (2008) used the IDP detector aboard the DEMETER satellite (Sauvaud et al., 2006) to identify times when the VLF transmitter located in the Northwest Cape of Australia (NWC) pitch-angle scattered electrons in the [100,400] keV energy range into the drift loss cone. They found that enhanced levels of flux were present in a narrow range of L-shells spanning [1.6,1.8] that depended on energy in the manner expected by the resonance condition at the heart of quasilinear theory. The average flux was plotted versus geographic longitude and latitude to show a "wisp" of enhanced flux that started just a few degrees West of the NWC transmitter and persisted eastward until the South Atlantic Anomaly (SAA), where the electrons were lost to the system. More than 80% of DEMETER orbits show flux enhancements in the drift loss cone associated with scattering of 100–400 keV electrons (Rodger et al., 2010). Members of that team also looked for enhanced fluxes from the NPM transmitter in Hawaii, which is at lower L-shell, and rarely saw them; the only example shown is for <250 keV electrons (Gamble et al., 2008). Gamble et al. (2008) concluded that the paucity of enhanced fluxes below L = 1.6 for both NWC and NPM may suggest that nonducted propagation is an inefficient mechanism for scattering electrons. Selesnick et al. (2013) showed that a diffusion model could quantitatively explain the NWC observations, and Zhang et al. (2016) used the MEPED instrument on NOAA's POES satellite to see enhanced fluxes due to NWC at lower energy, [30,100] keV, and at the higher L-shells [1.8,2.1] predicted by the resonance condition. Li et al. (2012) showed a small enhancement of 300–800 keV electrons at L = [1.9,1.95], also using DEMETER data, but did not show precipitation above 400 keV for L < 1.6, perhaps because they binned fluxes coarsely in two of the three variables (energy, L, and longitude/B) rather than binning with high resolution in all three variables as we do here.

In this paper, we demonstrate that enhanced fluxes due to NWC are observed in the drift loss cone for higher energy (500–800 keV) and lower L-shells, L = [1.4, 1.8] than described in earlier work. The observations presented here create an opportunity for comparison to models at energies closer to the MeV range, for which the decay times remain unexplained and direct observation of precipitation is more difficult to see due to less frequent occurrence of higher flux levels in the inner belt (Fennell et al., 2015; Ripoll et al., 2019). We bin PROBA-V Energetic Particle Telescope (EPT) flux observations by McIlwain L and local strength of the magnetic field, B, and compare the average flux seen as a function of (B,L) during periods when the NWC transmitter is on versus when it is off, showing significant enhancements in flux that are attributable to the transmitter and occur at the energy-dependent L-shells predicted by the resonance condition for ducted and nonducted NWC waves. We next average the flux over (B,L) bins using two nonoverlapping ranges in geographic longitude to demonstrate that the enhanced fluxes are due to electrons that exist in a transition zone between "permanently trapped" and "quasi-trapped." We also display the log of the average fluxes when the transmitter is on versus off, plotted versus geographic longitude and latitude. These plots reveal "diffuse wisps," similar to the "wisps" shown in Sauvaud et al. (2008) but displaced to lower L, broader in L, and more restricted in longitude to near the Western edge of the SAA.

2. Data and Analysis

2.1. PROBA-V EPT Data

PROBA-V is a three-axis stabilized vegetation-imaging satellite launched by the European Space Agency on 7 May 2013 to LEO polar orbit with an altitude of 820 km, inclination of 98.73°, and 10:30 a.m. nominal local time of the descending node (Pierrard et al., 2014). The EPT (Cyamukungu et al., 2014) is a (dE, E) charged-particle spectrometer using a thin front detector and thick back detector. The EPT accumulates counts in a large number of physical channels using deposited-energy thresholds, but estimates electron flux in only seven virtual channels spanning the following energy ranges (in MeV): E1 = [0.5,0.6], E2 = [0.6,0.7],

E3 = [0.7,0.8], E4 = [0.8,1], E5 = [1,2.4], E6 = [2.4,8], E7 = [8,20]. The collimator opening angle is 52° with the central axis pointed East on the nightside and West on the dayside. A three-component magnetometer determines the local magnetic field direction at the satellite allowing the pitch-angle corresponding to the look direction of the central axis to be computed and dumped to file. The files that were used for this study contain the date and time of collection, the geographic longitude and latitude, pitch-angle, McIlwain L of a particle that mirrors at the satellite location, B field at the satellite, the flux in each of the seven virtual channels, and a chi-squared fit value. The time cadence of the samples is 2 s. The McIlwain L and local B-field strength are evaluated using the UNILIB v2.20 (http://trend.aeronomie.be/NEEDLE/unilib.html) implementation of the IGRF/Olsen-Pfitzer quiet-time magnetic field model. Data from August–September, 2016, were used for this study for reasons explained below.

2.2. The NWC Transmitter

The NWC transmitter is located in the NWC at (21.82°S, 114.15°E), which corresponds to magnetic coordinates of (−31.96°, 186.4°) and an L-shell of ~1.4. The transmitter operates nearly continuously with ~1 MW radiated power, except for routine maintenance that occurs regularly on Monday/Wednesday mornings and sometimes on other days. Routine maintenance outages have a variable duration that is typically less than 8 hr, often significantly less than 8 hr. We used the ABOVE VLF receiver network (Cully et al., 2014) to identify a rare and extended maintenance period spanning 15 August (~02:30 UT) through 18 September 2016 during the entirety of which NWC was off. We call this period the "transmitter off" period in discussions below. The 2-week period prior to, and the 2-week period after, the extended maintenance period was used as the "transmitter on" period, and included the short outages due to routine maintenance. The extended maintenance period provides an ideal opportunity to compare EPT fluxes when the transmitter is "on" to when the transmitter is "off," particularly when the NWC is on the nightside where we expect to see an effect.

2.3. Analysis of the PROBA-V EPT Data

The EPT data were binned in several ways. First, we binned the data for each electron channel in (B,L) coordinates, with bins in B that are 0.01 Gauss wide and span [0.15,0.4] G, and bins in McIlwain L that are 0.04 R_E wide spanning [1.2,2]. We accumulated 2-s flux estimates in each (B,L) bin spanning the "transmitter on" and "transmitter off" periods. We did separate accumulations for times when NWC was on the dayside and nightside, anticipating from Sauvaud et al. (2008) that we would see a bigger effect when NWC is on the nightside than the dayside. Because Sauvaud et al. (2008) showed that enhanced fluxes were seen when the satellite was at longitudes between the NWC and the SAA, we also restricted our samples to be from times when PROBA-V was in this longitude range (120–300°E). We accumulated the number of flux samples in each (B,L) bin, as well as the flux, and computed the average flux in each (B,L) bin by dividing the accumulated flux by the number of samples in each (B,L) bin. In this way, we generated the information for the "transmitter on, dayside" and "transmitter on, nightside" figures in section 3. We followed this same prescription to find the average fluxes during the extended maintenance period to generate the information for the "transmitter off, dayside" and "transmitter off, nightside" figures. Finally, in order to test the hypothesis that the enhanced fluxes were caused by NWC scattering electrons into the drift loss cone, we generated a second set of average fluxes by accumulating flux only when the satellite was East of the SAA and well West of the NWC. The idea is that any flux seen at values of (B,L) that are in the drift loss cone at longitudes East of the SAA could not have been scattered to that value of B by the NWC transmitter because they would have been intercepted by the SAA prior to drifting to that location. In summary, then, for each energy channel, we generated eight average fluxes versus B and L under different conditions for the transmitter and locations for the satellite.

3. Enhanced Fluxes Show NWC Scattering of 500–800 keV Electrons Over L = 1.4–1.8

Figure 1a contains a comparison of the average flux for the [500,600] keV channel, in the L = [1.52,1.56] bin, as a function of B. The plot on the left shows the average flux when NWC is on the nightside for the "transmitter on" (black) and "transmitter off" (red) conditions, with the averaging further divided into times when the satellite longitude is either (a) between the NWC and SAA (120–300°E), i.e., the satellite is West of the

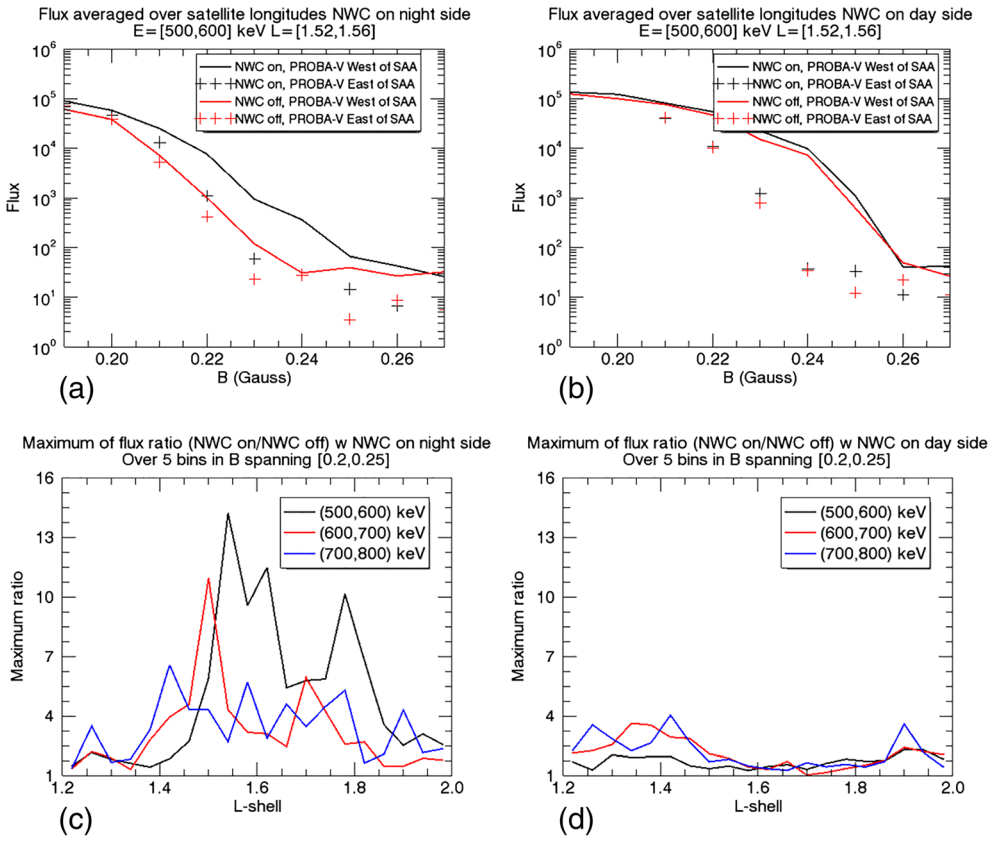

Figure 1. Average flux (electrons/cm^2 s sr MeV) for the [500,600] keV electron energy channel when NWC is on the (a) nightside and (b) dayside. Maximum ratio of the flux when the NWC transmitter is "on" to the flux when it is "off," over B spanning [0.2,0.25], when NWC is (c) on the nightside and (d) on the dayside, for three energy channels from EPT.

SAA (solid lines), or (b) the satellite is East of the SAA (plus symbols). Figure 1b shows the same information when NWC is on the dayside.

A comparison of the solid black and solid red lines in Figure 1a illustrates that when the NWC transmitter is on and in the nightside, the flux is enhanced relative to when the transmitter is off and in the nightside, for values of B spanning the interval [0.2,0.25]. There is no difference between the average fluxes when the transmitter is on versus off when the transmitter is on the dayside (Figure 1b). A comparison of the solid black line with the black symbols in Figure 1a shows that as much as 90% of the average flux for values of B in the range [0.22,0.25] is lost in the SAA, since the average flux when PROBA-V is West of the SAA (solid black line) is approximately nine times higher than when PROBA-V is East of the SAA (black symbols). This would appear to mean that electrons are being scattered by the NWC into the drift loss cone, the "quasi-trapped region," and most are lost when they encounter the SAA in less than one drift around Earth. A similar behavior is seen for the [600,700] and [700,800] keV channels (not shown), but for the higher energy channels (above 800 keV) the counting statistics are inadequate during the study interval to assess differences between the transmitter "on" and "off" average fluxes.

The value of B that we assign to the edge of the drift loss cone is the value for which an electron mirroring at that value drifts around Earth with a minimum altitude equal to 80 km. This value of B is L-dependent; at L = 1.54 in the IGRF magnetic field it is ~0.234 G. The value is also dependent on the minimum altitude. If we had used 200 km instead of 80 km, the value would be B = 0.224 G. Electrons that mirror at a value of B > 0.234 G will encounter an altitude lower than 80 km somewhere in their drift around Earth, e.g., in the SAA. Some of these electrons are in the drift loss cone and are called "quasi-trapped" because they are not expected to make a complete drift around Earth. Electrons that mirror at B < 0.234 are on drift shells that have a minimum altitude greater than 80 km, and are called "permanently trapped" because they are

expected to make multiple trips around Earth before they lose a significant fraction of their energy. Figure 1a illustrates that the edge of the drift loss cone is not a hard boundary, since the fraction of the enhanced flux that is lost in the SAA gradually increases with increasing B—there is not a discontinuous transition in the fraction that is lost at a single value of B. There is a substantial difference between the average flux when the transmitter is off and on the nightside (solid red line in Figure 1a) vs. the dayside (solid red line in Figure 1b). This may be due to the fact that the minimum altitude achieved by the drift shells is in the SAA, which is on the opposite side of Earth from NWC. Thus, when NWC is on the nightside, the SAA is on the dayside. Since the atmosphere and ionosphere are local-time dependent, the trapped flux has a diurnal dependence described in Cunningham et al. (2018), which we observe here.

In order to identify which L-shells show flux enhancements and which do not, for each bin in L we compute the ratio of the average flux when the NWC transmitter is "on" to the average flux when the NWC transmitter is "off," both taken when NWC is on the nightside, for each bin in B spanning the range [0.2,0.25]. The maximum of the five ratios thus obtained is plotted in Figure 1 as the "maximum ratio" versus L for each of three energy channels. We find enhancement in flux over several relatively narrow ranges in L (Figure 1c). When NWC is on the dayside (Figure 1d), we find that there is no significant enhancement in fluxes. The maximum ratio obtains a peak value at higher L for lower energy, consistent with previous work (Sauvaud et al., 2008; Zhang et al., 2016). The peak value of the maximum ratio obtained over all L is 7–13, much smaller than the factor of 300 that was reported for lower energies (Sauvaud et al., 2008), which may be due to the fact that the lower-energy observations were made at higher values of B where the "background" flux level is much lower. Figure 1c shows additional peaks of the maximum ratio at higher L-shell for each energy which were unexpected.

Figure 1 prompts the question of whether the peaks are at values of L where we expect resonant interactions with NWC transmitter waves to occur. We investigated this using a dipole magnetic field $\boldsymbol{B}(\boldsymbol{L},\lambda)$, where λ is magnetic latitude (MLAT), and a cold plasma density model $\boldsymbol{N}(\boldsymbol{L}) = \mathbf{3572}(\mathbf{1.5}/\boldsymbol{L})^{\mathbf{4}}$, which approximates the "low-density" model used by Starks et al. (2020). At L = 1.54, this density model is ~40% lower than that of Ozhogin et al. (2012), or about 1 standard deviation below the recommended value (Ozhogin et al., 2012, Equation 2). We use these models and the cold plasma dispersion relation to compute the index of refraction, $\boldsymbol{n}(\theta,\boldsymbol{L}) = \boldsymbol{ck}(\theta,\boldsymbol{L})/\omega$, where θ is the wave normal angle, $\boldsymbol{c}$ is the speed of light, $\boldsymbol{k}$ is the wave number, and ω is the NWC wave frequency (19.8 kHz). We are interested in waves that scatter electrons that mirror near the edge of the drift loss cone, which we specify as mirroring at a fixed value of B = 0.22 G, the center of the range used to compute the maximum flux ratios in Figures 1c/1d. The resonance condition (Glauert & Horne, 2005) can be expressed as

$$\boldsymbol{n}(\theta,\boldsymbol{L})\cos\theta = \left(\mathbf{1} + \frac{\boldsymbol{m}|\boldsymbol{\Omega_e}|}{\gamma\omega}\right) / \left(\cos\alpha_{eq}\sqrt{\mathbf{1} - (\mathbf{1}/\gamma)^2}\right), \tag{1}$$

where $|\boldsymbol{\Omega_e}(\boldsymbol{L})|$ is the nonrelativistic electron gyrofrequency, $\cos\alpha_{eq} = \sqrt{\mathbf{1} - (\boldsymbol{B}(\boldsymbol{L},\lambda)/\mathbf{0.22})}$ is the cosine of the equatorial pitch-angle, and $\gamma = \mathbf{1} + (\boldsymbol{E}/\boldsymbol{m_e c^2})$ is the Lorentz factor for an electron with kinetic energy $\boldsymbol{E}$. Thus, for fixed values of $\boldsymbol{E}$, $\boldsymbol{L}$, λ and the "harmonic number" $\boldsymbol{m}$, we find the values of θ that satisfy Equation 1. If there is more than one value of θ that satisfies 1, we retain the solution that is closest to parallel; there may be no solutions at some ($\boldsymbol{E}$, $\boldsymbol{m}$, $\boldsymbol{L}$, λ). In this manner we compute $\theta(\boldsymbol{E}, \boldsymbol{m}, \boldsymbol{L}, \lambda)$ as the solution to a root-finding problem, an example of which is in Figure 2a for $\boldsymbol{E} = \mathbf{500}$, $\boldsymbol{m} = \pm\mathbf{1}$, $\boldsymbol{L} = \mathbf{1.75}$, $\lambda = \mathbf{0}$.

For the three energy channels plotted in Figures 1c/1d, we find that a parallel wave at the magnetic equator with $\boldsymbol{m} = -1$ is resonant for values of L near the primary peaks in Figure 1c, plotted as colored circles in Figure 2b. We also find that for the secondary peaks in Figure 1c the resonance condition is satisfied for a more oblique wave at the magnetic equator with $\boldsymbol{m} = +1$ (colored rectangles in Figure 2b). Resonant interactions with NWC waves may also occur off the magnetic equator, although in Figure 2c we see that only a parallel wave interacting at the equator is resonant with 500 keV electrons at the L-shell where the primary peak occurs in Figure 1c (L = 1.54). Thus, at lower L the electrons appear to be resonant with waves that are nearly parallel, typically associated with ducted propagation. At the higher L associated with the secondary peaks (1.65–1.8), both parallel and oblique waves can be resonant, with oblique waves resonant near the equator for $\boldsymbol{m} = +1$ and parallel waves resonant off-equator for $\boldsymbol{m} = \pm\mathbf{1}$. Due to the fact that the

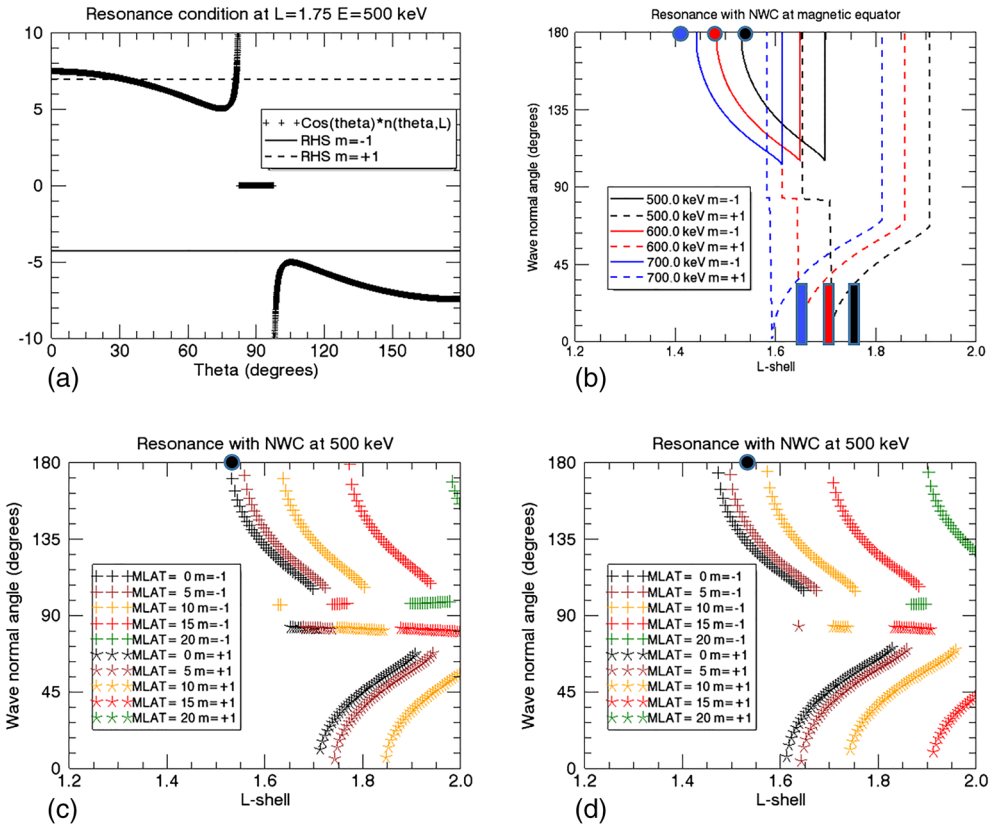

Figure 2. (a) Resonance condition for NWC waves at $E = 500$, $m = \pm 1$, $L = 1.75$, $\lambda = 0$ shows a solution for $m = +1$ (dashed horizontal line) but not $m = -1$ (solid horizontal line). (b) Wave normal angles satisfying the resonance condition at the magnetic equator for three energies. The colored circles (rectangles) are centered at the L-shell where the largest (secondary) peaks for each energy are seen in Figures 1c/1d. Wave normal angles satisfying the resonance condition at $E = 500$ keV as a function of L, λ using the (c) low-density plasma model and (d) low-density plasma model multiplied by 1.4.

transmitter is a significant distance from the footpoints associated with these larger L-shells, we think it more likely that oblique waves associated with nonducted propagation from the NWC transmitter are responsible for the scattering observed at larger L. The density model that is used affects this interpretation, since an increase in density shifts the solutions to lower L and makes a resonant interaction with oblique waves possible at lower L. Figure 2d shows the result when the density model is multiplied by 1.4, bringing it to the value recommended by Ozhogin et al. (2012) at L = 1.54. Lyons et al. (1972) and Glauert and Horne (2005) showed that the $m = -1$ and $m = +1$ harmonics can have comparably sized diffusion coefficients, while Mourenas and Ripoll (2012) showed that harmonics with $|m| > 1$ are associated with small diffusion coefficients at L = 1.5. Ripoll et al. (2014) has comprehensive figures of diffusion coefficients and electron lifetimes as a function of ω, θ, E, m, L due to narrowband waves.

The average flux can also be plotted as a function of geographic latitude and longitude. In Sauvaud et al. (2008), this type of plot shows a "wisp" of enhanced flux along a curved line that corresponds to a fixed McIlwain L-shell and extends over a broad range of longitude from the NWC transmitter East to the SAA. The wisps in Sauvaud et al. (2008) were not observed East of the SAA. We do not see a pronounced narrow wisp spanning a wide range of longitude, but we do see a "diffuse wisp" of enhanced flux West of the SAA at energy-dependent L-shells (Figure 3). The diffuse wisp is displaced to lower L, is broader in L, and is more restricted in longitude to near the Western edge of the South Atlantica Anomaly (SAA) than the "wisps" seen in Sauvaud et al. (2008).

Now we anticipate some concerns that the reader may have with our analysis. First, the large opening angle of the collimator, combined with the fact that the collimator points East on the nightside and West on the

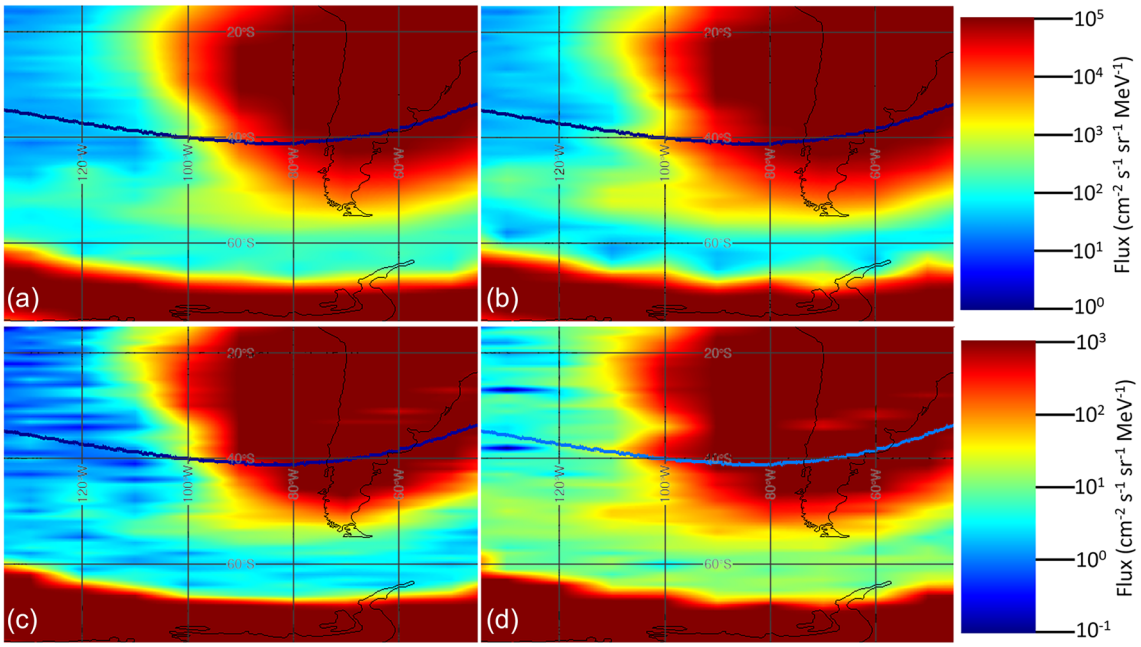

Figure 3. (top) Logarithm of the average flux in the [500,600] keV channel (spanning 1–10^5 electrons/cm^2 s sr MeV) as a function of geographic longitude (horizontal) and latitude (vertical) when NWC is on the nightside and the transmitter is (a) off and (b) on. (bottom) Same as (top) but for the average flux in the [600,700] keV channel (spanning 0.1–10^3 electrons/cm^2 s sr MeV) when the transmitter is (c) off and (d) on. The outer radiation belt is the dark red band at the bottom of each image. The SAA is the dark area of red encompassing the bottom half of South America. The curved thick line is L = 1.54.

dayside, may create a systematic bias in the range of local pitch angles that is accepted by the collimator aperture. We generated the results in Figures 1a/1b using two approaches, one which used only local pitch-angles within 5° of 90 and used the B at the satellite location as is, and a second approach that used all pitch angles but corrected B by dividing it by the squared sine of the local pitch angle. The two approaches produced no substantive differences (not shown). Second, the magnetic field model used to evaluate (B,L) does not include effects from solar or geomagnetic activity. We evaluated a variety of field models that include these effects and found that the strength of the field varies in the third significant digit (~100 nT) during our study period, and is thus inconsequential (not shown). Third, it is possible that the permanently trapped population of electrons could vary with time. We computed the daily-averaged value of the "most trapped" population sampled by the PROBA-V satellite at L = [1.52,1.56], and found that it varies by less than a factor of ±2 from its mean value over the 60-day study period (not shown). The fact that the flux of [500,600] keV electrons is so steady over this period is likely due to the fact that cosmic-ray albedo neutron decay is a steady source of the electron population at this energy and L-shell that reaches an equilibrium state in the absence of injections (Xiang et al., 2019). Finally, we emphasize that we only consider scattering by NWC in Figure 2 because the flux ratio is a comparison of times when NWC is on versus off; however, it is possible that some of the scattering observed by PROBA-V is caused by other transmitters.

Our interpretation that the resonant waves at lower L (1.48–1.54) are parallel, likely associated with ducted transport, and that the resonant waves at larger L (1.65–1.75) may be oblique, associated with non-ducted transport, might surprise the reader. While the results shown here do not specify the relative abundance of ducted vs. nonducted waves at any L, our interpretation relies on the possibility of ducts existing down to L = 1.48. Thomson (1987a) studied ducted and nonducted waves that were received at Dunedin from the NPM transmitter in Hawaii by measuring the group delay. The occurrence histogram of group delays (Thomson, 1987a, Figure 4) shows two distinct received signal populations. The first population has a narrow peak at ~100 ms and was shown by Thomson (1987b) to be nonducted whistlers reaching a maximum height of 1,400 km. The second population, "normal whistlers" assumed to be ducted, has a peak at ~450 ms and extends from ~200 to ~800 ms. This range of group delays corresponds to an L-shell range of ~[1.5,3] using an offset dipole and the Ozhogin et al. (2012) cold plasma density model

(with latitude dependence) to compute the total delay, i.e., the integral along the field line of the arclength divided by the local group velocity, $\partial\omega/\partial k$, for a parallel wave. Clilverd et al. (2008) states that ducting is not observed below L ~ 1.5 based on Thomson (1987a, 1987b), presumably using such an analysis. This is in conflict with our assertion that ducted waves at L = [1.48,1.54] are responsible for the enhanced fluxes observed by NWC; however, increasing the cold plasma density by a factor of 2 (well within the uncertainty in Ozhogin et al., 2012, Equation 2) means that the 200 msec delay is consistent with L = 1.3, eliminating the conflict. Clilverd et al. (2008) found that the DEMETER-measured spatial distribution of wave power measured directly above NWC was centered on the transmitter after correction for field line geometry, but the spatial distribution of power in the conjugate hemisphere was offset poleward, consistent with propagation of oblique waves. A spatial distribution of power above the transmitter and at its conjugate point that are very similar would be consistent with ducted propagation. Cohen and Inan (2012) observed distributions consistent with ducted propagation at low L and nonducted propagation at high L for NWC using DEMETER.

Starks et al. (2020, Figure 11) compare predicted electric and magnetic field intensities versus L-shell, summed over all nine transmitters they modeled and averaged over season, local time, and magnetic longitude, to data from Ma et al. (2017) and Meredith et al. (2019). They conclude that the low-density nonducted model best matches the data for L < 1.7 and the high-density ducted model best matches for L > 1.7. This appears to contradict our interpretation of the NWC data, although it should be emphasized that Figure 11 in Starks et al. (2020) is the cumulative intensity from all nine transmitters, whereas our study concerns only NWC. More importantly, if one matches the location of the peak intensity in L, rather than the value of the peak intensity, the ducted model is a better match at L < 1.7 because it has a peak at L = 1.5, whereas the nonducted model has a peak near L = 1.25 (see also the predictions for NWC in Starks et al., 2020, Figures 5 and 6). For this reason, we interpret the model results of Starks et al. (2020) as supporting our interpretation of the NWC data. Starks et al. (2020, Figure 9) show that the ducted and nonducted models for NWC yield comparable intensity at L = 1.6, suggesting that both ducted and nonducted waves may have adequate intensity to scatter electrons at higher L.

4. Conclusions

PROBA-V EPT data have been used to quantify the effect that pitch-angle scattering from the NWC transmitter has on average fluxes of [500,800] keV electrons over (B, L). We observe enhanced average fluxes when NWC is "on" compared to when it is "off," but only when NWC is on the nightside. No significant change in average flux is observed when NWC is on the dayside. The ratio of flux computed with the transmitter "on" versus "off" shows multiple peaks for each energy channel, each peak spanning a narrow range in L. The primary peak for higher energies is centered at lower L while for lower energies the peak is centered at higher L, consistent with Sauvaud et al. (2008) and Zhang et al. (2016) for lower energies. Secondary peaks follow the same pattern but displaced to higher L. We calculated the resonance condition between the NWC transmitter waves and electrons that mirror at the edge of the quasi-trapped region, and found that a parallel wave most likely explains the primary peaks at low L and an oblique wave most likely explains the secondary peaks at higher L for each of the three energy channels. This is consistent with modeling by Starks et al. (2020), who showed that powerful ducted waves can exist for L < 1.5 from NWC, but the power from nonducted waves gradually overtakes that of ducted waves as L increases. Whereas Gamble et al. (2008) failed to identify observations of enhanced flux at L < 1.6 due to NWC, here we show enhanced fluxes down to L ~ 1.4 for the first time. We are not aware that secondary peaks at higher L-shell have been reported previously.

The enhanced fluxes are observed at values of B for which the electrons are in a transition zone between "permanently trapped" and "quasi-trapped," which we appear to be probing with the observations shown here. The enhanced fluxes are observed immediately West of the SAA, but the enhanced flux level is reduced at the same value of B East of the SAA, which suggests that interactions with the atmosphere in the SAA has removed most of these electrons. The fraction of the enhanced flux that is lost drifting East through the SAA gradually increases with increasing B, reinforcing the idea that there is a gradual transition from "permanently trapped" to "quasi-trapped," and that the edge of the drift loss cone is not a hard boundary. We defer to future work the use of a model to reproduce the observations, including the gradual transition from "permanently trapped" to "quasi-trapped."

Acknowledgments

The authors thank the International Space Sciences Institute (ISSI) and the participants in a 2020 ISSI workshop, during which this work began. GC was supported by the Laboratory Directed Research and Development program of Los Alamos National Laboratory under project 20200073DR. The work by GC and JFR was performed under the auspices of an agreement between CEA/DAM and NNSA/DP in cooperation on fundamental science. EPT data are publicly available at the ESA website (http://swe.ssa.esa.int/space-radiation). EB and VP thank STCE (Solar Terrestrial Center of Excellence) and funding from the Research Executive Agency under the European Union's Horizon 2020 Research and Innovation program (project SafeSpace). CC acknowledges the support of the Natural Sciences and Engineering Research Council of Canada (NSERC). The ABOVE VLF receiver network is supported by the Canada Foundation for Innovation and the Canadian Space Agency. ABOVE data are available online (https://data.phys.ucalgary.ca/sort_by_project/GO-Canada/GO-ABOVE/).

References

Abel, B., & Thorne, R. M. (1998). Electron scattering loss in Earth's inner magnetosphere 1. Dominant physical processes. *Journal of Geophysical Research*, *103*(A2), 2385–2396. https://doi.org/10.1029/97JA02919

Albert, J. M., Starks, M. J., Selesnick, R. S., Ling, A. G., O'Malley, S., & Quinn, R. A. (2020). VLF transmitters and lightning-generated whistlers: 2. Diffusion of radiation belt electrons. *Journal of Geophysical Research: Space Physics*, *125*, e2019JA027030. https://doi.org/10.1029/2019JA027030

Claudepierre, S. G., Ma, Q., Bortnik, J., O'Brien, T. P., Fennell, J. F., & Blake, J. B. (2020). Empirically estimated electron lifetimes in the Earth's radiation belts: Van Allen Probe observations. *Geophysical Research Letters*, *47*, e2019GL086053. https://doi.org/10.1029/2019GL086053

Clilverd, M. A., Rodger, C. J., Gamble, R., Meredith, N. P., Parrot, M., Berthelier, J.-J., & Thomson, N. R. (2008). Ground-based transmitter signals observed from space: Ducted or nonducted? *Journal of Geophysical Research*, *113*, A04211. https://doi.org/10.1029/2007JA012602

Cohen, M. B., & Inan, U. S. (2012). Terrestrial VLF transmitter injection into the magnetosphere. *Journal of Geophysical Research*, *117*, A08310. https://doi.org/10.1029/2012JA017992

Cully, C. M., Chaddock, D., Daniel, C., Davis, E., Galts, D., McGuffin, N., et al. (2014). Early results on energetic particle precipitation observed by the ABOVE instrument array, Abstract SA13B-3997 presented at 2014 Fall Meeting, AGU, San Francisco, Calif., 15-19 Dec.

Cunningham, G. S., Loridan, V., Ripoll, J.-F., & Schulz, M. (2018). Neoclassical diffusion of radiation-belt electrons across very low L-shells. *Journal of Geophysical Research: Space Physics*, *123*, 2884–2901. https://doi.org/10.1002/2017JA024931

Cyamukungu, M., Benck, S., Borisov, S., Bonnet, L., Grégoire, G., Cabrera, J., et al. (2014). The Energetic Particle Telescope (EPT) on board Proba-V: Description of a new science-class instrument for particle detection in space. *IEEE Transactions on Nuclear Science*, *61*(6), 3667–3681. https://doi.org/10.1109/TNS.2014.2361955

Fennell, J. F., Claudepierre, S. G., Blake, J. B., O'Brien, T. P., Clemmons, J. H., Baker, D. N., et al. (2015). Van Allen Probes show that the inner radiation zone contains noMeV electrons: ECT/MagEIS data. *Geophysical Research Letters*, *42*, 1283–1289. https://doi.org/10.1002/2014GL062874

Gamble, R. J., Rodger, C. J., Clilverd, M. A., Sauvaud, J.-A., Thomson, N. R., Stewart, S. L., et al. (2008). Radiation belt electron precipitation by man-made VLF transmissions. *Journal of Geophysical Research*, *113*, A10211. https://doi.org/10.1029/2008JA013369

Glauert, S. A., & Horne, R. B. (2005). Calculation of pitch angle and energy diffusion coefficients with the PADIE code. *Journal of Geophysical Research*, *110*, A04206. https://doi.org/10.1029/2004JA010851

Li, X., Ma, Y., Wang, P., Wang, H., Lu, H., Zhang, X., et al. (2012). Study of the North West Cape electron belts observed by DEMETER satellite. *Journal of Geophysical Research*, *117*, A04201. https://doi.org/10.1029/2011JA017121

Lyons, L. R., & Thorne, R. M. (1973). Equilibrium structure of radiation belt electrons. *Journal of Geophysical Research*, *78*(13).

Lyons, L. R., Thorne, R. M., & Kennel, C. F. (1972). Pitch-angle diffusion of radiation belt electrons within the plasmasphere. *Journal of Geophysical Research*, *77*(19), 3455–3474. https://doi.org/10.1029/JA077i019p03455

Ma, Q., Mourenas, D., Li, W., Artemyev, A., & Thorne, R. M. (2017). VLF waves from ground-based transmitters observed by the Van Allen Probes: Statistical model and effects on plasmaspheric electrons. *Geophysical Research Letters*, *44*, 6483–6491. https://doi.org/10.1002/2017GL073885

Mauk, B. H., Fox, N. J., Kanekal, S. G., Kessel, R. L., Sibeck, D. G., & Ukhorskiy, A. (2012). Science objectives and rationale for the Radiation Belt Storm Probes mission. *Space Science Reviews*, *179*(1-4), 3–27. https://doi.org/10.1007/s11214-012-9908-y

Meredith, N. P., Horne, R. B., Clilverd, M. A., & Ross, J. P. J. (2019). An investigation of VLF transmitter wave power in the inner radiation belt and slot region. *Journal of Geophysical Research: Space Physics*, *124*, 5246–5259. https://doi.org/10.1029/2019JA026715

Mourenas, D., & Ripoll, J.-F. (2012). Analytical estimates of quasi-linear diffusion coefficients and electron lifetimes in the inner radiation belt. *Journal of Geophysical Research*, *117*, A01204. https://doi.org/10.1029/2011JA016985

Ozhogin, P., Tu, J., Song, P., & Reinisch, B. W. (2012). Field-aligned distribution of the plasmaspheric electron density: An empirical model derived from the IMAGE RPI measurements. *Journal of Geophysical Research*, *117*, A06225. https://doi.org/10.1029/2011JA017330

Pierrard, V., Lopez Rosson, G., Borremans, K., Lemaire, J., Maes, J., Bonnewijn, S., et al. (2014). The energetic particle telescope: First results. *Space Science Reviews*, *184*(1–4), 87–106. https://doi.org/10.1007/s11214-014-0097-8

Ripoll, J.-F., Albert, J. M., & Cunningham, G. S. (2014). Electron lifetimes from narrowband wave-particle interactions within the plasmasphere. *Journal of Geophysical Research: Space Physics*, *119*, 8858–8880. https://doi.org/10.1002/2014JA020217

Ripoll, J.-F., Claudepierre, S. G., Ukhorskiy, A. Y., Colpitts, C., Li, X., Fennell, J., & Crabtree, C. (2020). Particle dynamics in the Earth's radiation belts: Review of current research and open questions. *Journal of Geophysical Research: Space Physics*, *125*, e2019JA026735. https://doi.org/10.1029/2019JA026735

Ripoll, J.-F., Loridan, V., Denton, M. H., Cunningham, G., Reeves, G., Santolík, O., et al. (2019). Observations and Fokker-Planck simulations of the L-shell, energy, and pitch angle structure of Earth's electron radiation belts during quiet times. *Journal of Geophysical Research: Space Physics*, *124*, 1125–1142. https://doi.org/10.1029/2018JA026111

Rodger, C. J., Carson, B. R., Cummer, S. A., Gamble, R. J., Clilverd, M. A., Green, J. C., et al. (2010). Contrasting the efficiency of radiation belt losses caused by ducted and nonducted whistler-mode waves from ground-based transmitters. *Journal of Geophysical Research*, *115*, A12208. https://doi.org/10.1029/2010JA015880

Ross, J. P. J., Meredith, N. P., Glauert, S. A., Horne, R. B., & Clilverd, M. A. (2019). Effects of VLF transmitter waves on the inner belt and slot region. *Journal of Geophysical Research: Space Physics*, *124*, 5260–5277. https://doi.org/10.1029/2019JA026716

Sauvaud, J.-A., Maggiolo, R., Jacquey, C., Parrot, M., Berthelier, J.-J., Gamble, R. J., & Rodger, C. J. (2008). Radiation belt electron precipitation due to VLF transmitters: Satellite observations. *Geophysical Research Letters*, *35*, L09101. https://doi.org/10.1029/2008GL033194

Sauvaud, J.-A., Moreau, T., Maggiolo, R., Treilhou, J.-P., Jacquey, C., Crosa, A., et al. (2006). High-energy electron detection onboard DEMETER: The IDP spectrometer, description and first results on the inner belt. *Planetary and Space Science*, *54*(5), 502–511. https://doi.org/10.1016/j.pss.2005.10.019

Selesnick, R. S., Albert, J. M., & Starks, M. J. (2013). Influence of a ground-based VLF radio transmitter on the inner electron radiation belt. *Journal of Geophysical Research: Space Physics*, *118*, 628–635. https://doi.org/10.1002/jgra.50095

Starks, M. J., Albert, J. M., Ling, A., O'Malley, S., & Quinn, R. A. (2020). VLF transmitters and lightning-generated whistlers: 1. Modeling waves from source to space. *Journal of Geophysical Research: Space Physics*, *125*, e2019JA027029. https://doi.org/10.1029/2019JA027029

Thomson, N. R. (1987a). Experimental observations of very low latitude man-made whistler-mode signals. *Journal of Atmospheric and Terrestrial Physics*, *49*(4), 309–319. https://doi.org/10.1016/0021-9169(87)90027-4

Thomson, N. R. (1987b). Ray tracing the paths of very low latitude whistler-mode signals. *Journal of Atmospheric and Terrestrial Physics*, *49*(4), 321–338. https://doi.org/10.1016/0021-9169(87)90028-6

Xiang, Z., Li, X., Selesnick, R., Temerin, M. A., Ni, B., Zhao, H., et al. (2019). Modeling the quasi-trapped electron fluxes from cosmic ray albedo neutron decay (CRAND). *Geophysical Research Letters*, *46*, 1919–1928. https://doi.org/10.1029/2018GL081730

Zhang, Z., Li, X., Wang, C.-Y., & Chen, L. J. (2016). North west cape-induced electron precipitation and theoretical simulation. *Chinese Physics B*, *25*(11). https://doi.org/10.1088/1674-1056/25/11/119401